This article has been accepted for publication in IEEE Transactions on Mobile Computing. This is the author's version which has not been fully edited and
content may change prior to final publication. Citation information: DOI 10.1109/TMC.2024.3452499

MagWear: Vital Sign Monitoring based on Biomagnetism Sensing

Xiuzhen Guo, *Member IEEE,* Long Tan, *Student Member IEEE,* Chaojie Gu, *Member IEEE,*
Yuanchao Shu, *Member IEEE,* Shibo He, *Member IEEE,* Jiming Chen, *Fellow IEEE*

Abstract—This paper presents the design, implementation, and evaluation of MagWear, a novel biomagnetism-based system that can accurately and inclusively monitor the heart rate, respiration rate, and blood pressure of users. MagWear's contributions are twofold. Firstly, we build a mathematical model that characterizes the magnetic coupling effect of blood flow under the influence of an external magnetic field. This model uncovers the variations in accuracy when monitoring vital signs among individuals. Secondly, leveraging insights derived from this mathematical model, we present a software-hardware co-design that effectively handles the impact of human diversity on the performance of vital sign monitoring, pushing this generic solution one big step closer to real adoptions. Following IRB protocols, our extensive experiments involving 30 volunteers demonstrate that MagWear achieves high monitoring accuracy with a mean percentage error (MPE) of 1.55% for heart rate (HR), 1.79% for respiration rate (RR), 3.35% for systolic blood pressure (SBP), and 3.89% for diastolic blood pressure (DBP). MagWear can also be extended to detect anemia and blood oxygen saturation, which is also our ongoing work. Code and hardware schematics can be found at: https://github.com/tanwork/MagWear.

Index Terms—Wearable Health, Mobile Computing, Magnetic Sensing

◆

1 INTRODUCTION

Vital sign monitoring, such as tracking the heart rate (HR) and respiration rate (RR), has become a popular functionality on smart wearables. By continuously monitoring the vital signs of the wearer, these wearable devices enable a broad spectrum of health-care applications, including sleep monitoring, fitness tracking, and health issue alerting.

Nowadays, smartwatches [1], [2], [3] have emerged as the primary choice for continuous vital sign monitoring among various types of wearables. These smartwatches adopt Photoplethysmography (PPG) sensor that emits an LED beam onto the skin. The LED signal is mirrored back based on the blood volume circulating through the wrist's veins. The PPG waveform contains the pattern of the blood volume variations occurring between the systolic and diastolic phases of the cardiac cycle. The frequency of the PPG signal reflects the heart rate (HR) and respiration rate (RR). We can further leverage the filter to separate these two vital signs.

Despite their convenience, existing PPG-based smartwatches still face several crucial challenges that limit their ability to accurately monitor vital signs across diverse populations.

- Firstly, PPG sensors are shown to be less accurate in people with dark skin [4]. This discrepancy arises due to the elevated melanin levels in darker skin, causing absorption of the laser light and consequently reducing the signal-to-noise ratio of the measurements.
- Secondly, PPG sensors often need to be worn snugly against the skin to ensure accurate readings. This can lead to discomfort, skin irritation, or even pressure-related discomfort when used for extended periods [5].
- Thirdly, the PPG sensor's accuracy can be affected by temperature variations and moisture levels of the skin, potentially leading to fluctuations in readings [6].

To overcome these issues, prior works have put forth the idea of harnessing *biomagnetism* as an alternative approach for monitoring human vital signs [7], [8]. This approach is based on a physiological process where the blood circulation within the body during each heartbeat gives rise to the movement of charged particles (ions). These ions, in turn, induce a biomagnetic field, the strength of which corresponds to the fluctuations occurring with each individual heartbeat.

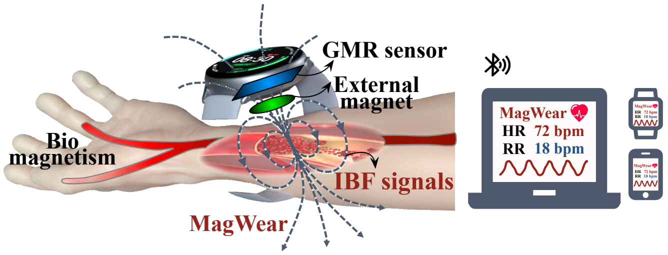

Fig. 1. An illustration of MagWear. A built-in tiny magnet pushes the blood flow to generate induced biomagnetic field (IBF) signals. MagWear then leverages a GMR sensor to detect subtle changes in IBF signals to derive the vital signs of HR, RR, and BP [9].

Some recent investigations [10], [7] have demonstrated the potential of such an approach. However, these studies face two major challenges: *i) Usability:* Many prior studies utilize fixed deployments for both users and measuring devices. This choice stems from the exceedingly weak induced biomagnetic field, necessitating meticulous tuning of sensing parameters to ensure the capture of adequate vital information across different users. The fixed deployment serves to mitigate uncertainties introduced by factors like the distance between the user and the device. Unfortunately, this method restricts its applicability primarily to lab environments and degrades the user experience. *ii) Reliability:* Measurements from prior studies show considerable inconsistencies. The correlation between system performance and individual-specific factors like wrist size, fat thickness, and blood vessel dimensions is still not fully understood. Consequently, systems may yield unreliable results when assessing a black-box modeling

Authorized licensed use limited to: Zhejiang University. Downloaded on October 30,2024 at 06:35:33 UTC from IEEE Xplore. Restrictions apply.
© 2024 IEEE. Personal use is permitted, but republication/redistribution requires IEEE permission. See https://www.ieee.org/publications/rights/index.html for more information.

This article has been accepted for publication in IEEE Transactions on Mobile Computing. This is the author's version which has not been fully edited and content may change prior to final publication. Citation information: DOI 10.1109/TMC.2024.3452499

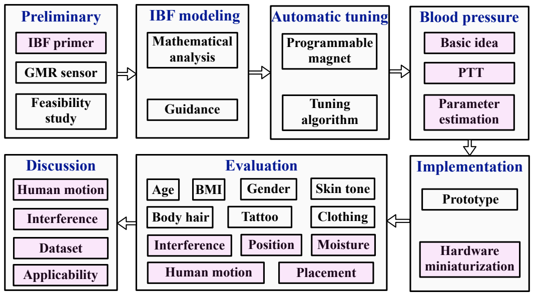

Fig. 2. The diagram of MagWear. The difference between the journal version and the MobiCom version [9] has been highlighted.

signal without a pragmatic methodology. In light of these challenges, substantial work remains before a wearable prototype can be developed for practical daily *in-situ* monitoring.

In this paper, we revisit biomagnetism and present the design, implementation, and evaluation of MagWear, the first wearable form factor design for inclusive and reliable vital sign monitoring. Figure 1 shows an illustration of MagWear, where a built-in tiny magnet pushes the blood flow to generate induced biomagnetic field (IBF) signals. MagWear then leverages a GMR sensor to detect subtle changes in IBF signals to derive the heart rate and respiration rate. To deal with the human diversity, MagWear adaptively optimizes the external excitation magnetic field to improve the SNR of IBF signals receptions, without human intervention.

The design of MagWear faces three practical challenges.

Absence of IBF signals modeling: To date, the theoretical and practical limits of biomagnetism for human vital sign monitoring are still largely unknown. More precisely, while previous research has demonstrated the possibility of capturing slight variations in the IBF signals through giant magnetoresistance (GMR) sensors, the reasons behind the varying precision of measurements among different individuals continue to elude us. The factors causing a GMR sensor configuration to succeed in one person while proving ineffective in another remain unclear. To this end, we thoroughly analyze the generation process of IBF signals and subsequently construct a comprehensive mathematical model that serves as a theoretical foundation guiding the design of MagWear.

Addressing user-dependent IBF signals variations: Once a comprehensive understanding is gained regarding the reasons underlying the variability of measurement accuracy among different individuals, the subsequent challenge is addressing this diversity inherent to humans. A fixed GMR sensor configuration inevitably leads to a deterioration in vital sign monitoring accuracy. To mitigate the influence introduced by individual distinctions, we propose an online adaptive algorithm that takes the IBF signal as the feedback and automatically adjusts the sensor configurations to improve the measurement accuracy, without explicit human intervention.

Wearable integration and prototyping: As a wearable, MagWear should balance an intricate interplay of detection accuracy, power consumption, and costs. We tackle this challenge by carefully designing both the hardware layout and signal processing pipeline. Our design offloads most of the signal processing to the analog domain, striking a balance between cost and power consumption. The hardware design, on the other hand, takes into account the impact of the magnet's position on measurement accuracy to optimize the overall layout. We expect the form factor of the current prototype can be largely reduced when implemented on a flexible PCB.

In addition to the heart rate and the respiration rate, we further extend MagWear to achieve the blood pressure monitoring by using the Pulse Transition Time (PTT). We introduce a set of signal processing methods to obtain the PTT accurately and reduce the parameter estimation errors (§5).

We conduct extensive experiments to evaluate the performance of MagWear in various settings. The evaluation involves 30 volunteers of diverse ages and skin tones. The field studies show that MagWear achieves consistently high performance with a mean percentage error (MPE) at 1.55% for heart rate (HR), 1.79% for respiration rate (RR), 3.35% for systolic blood pressure (SBP), and 3.89% for diastolic blood pressure (DBP). The head-to-head comparison of HR monitoring with the commodity Apple Watch 8 shows that MagWear respectively brings reductions in estimation error, particularly in scenarios involving diverse skin tones (up to 3.8×), body hair (up to 2.6×), tattoos (up to 2.1×), and clothing (up to 6.7×).

The contributions of this paper are summarized as follows.

- We build the first mathematical model that characterizes the magnetic coupling effect of blood flow under the influence of an external magnetic field. This model clarifies the variations in measurement accuracy observed among individuals and provides valuable guidance to improve the robustness of MagWear.
- We propose a power-efficiency hardware-software solution that can effectively handle the human diversity on biomagnetism-based vital sign monitoring performance, including HR, RR, and BP monitoring. The proposed solution pushes this inclusive vital sign monitoring solution one big step closer to real adoptions.
- We implement MagWear on a one-layer PCB board and follow the IRB protocol to conduct an extensive experiment involving 30 volunteers. The results confirm the superiority and inclusiveness of our proposed solution in both heart rate, respiration rate, and blood pressure monitoring when compared to the Apple Watch 8 baseline.

Difference with the conference version. Compared with the published MobiCom version [9] shown in Figure 2, we extend MagWear to achieve blood pressure (BP) estimation. In section 5, we introduce the basic idea of MagWear for BP estimation by using the Pulse Transition Time (PTT), and then propose a deep learning-based method to estimate systolic blood pressure (SBP) and diastolic blood pressure (DBP). We further make an effort to the device miniaturization. In section 6, we reimplement the prototype of MagWear and miniaturize its form factor. In Section 7, we evaluate MagWear's performance in BP estimation. We add another metric of the Bland-Altman Diagram to evaluate the agreement between HR, RR, and BP estimated with MagWear and the ground truth. In addition, we evaluate MagWear's performance under different electromagnetic interference. Finally, we discuss the limitation of MagWear in Section 9.

2 PRELIMINARY

MagWear explores biomagnetism, particularly the induced biomagnetic field (IBF) signals for human vital sign monitoring. In this section, we first present an overview of IBF signals (§2.1). We then detail the approach used for vital sign monitoring based on IBF signals (§2.2). Lastly, we summarize the key difficulties in implementing IBF-based vital sign monitoring by conducting thorough benchmarks (§2.3).

Authorized licensed use limited to: Zhejiang University. Downloaded on October 30,2024 at 06:35:33 UTC from IEEE Xplore. Restrictions apply.
© 2024 IEEE. Personal use is permitted, but republication/redistribution requires IEEE permission. See https://www.ieee.org/publications/rights/index.html for more information.

This article has been accepted for publication in IEEE Transactions on Mobile Computing. This is the author's version which has not been fully edited and content may change prior to final publication. Citation information: DOI 10.1109/TMC.2024.3452499

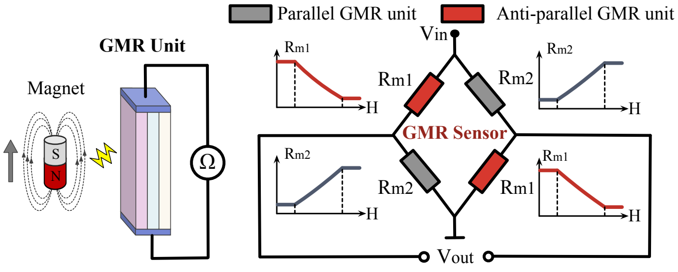

(a) GMR Unit (b) GMR Sensor

Fig. 3. Structure of (a) GMR unit and (b) GMR sensor.

2.1 Induced Biomagnetic Field Signals Primer

Generation of IBF signals. As an integral component of the human cardiovascular system, arteries serve as the conduits through which oxygen-rich blood is transported from the heart to every cell in the body. In arteries, there exists a large number of hemoglobin ($C_{3032}H_{4816}O_{812}N_{780}S_8Fe_4$), which is a protein found in red blood cells (RBCs) and plays a pivotal role in oxygen transport. This functionality stems from its ability to bind oxygen to its iron component in the Fe^{2+} state. Consequently, when subjected to an external magnetic field, the iron within hemoglobin in RBCs becomes magnetically attracted, resulting in an **induced biomagnetic field (IBF)** signals as elucidated by the principles of biomagnetism [11].

Relationship between IBF signals and vital signs. The strength of IBF signals corresponds to the fluctuations occurring with each individual heartbeat. The variation of IBF signals reflects cardiovascular activities and thus can be leveraged to monitor human vital signs. For instance, the heart continuously contracts and relaxes, while the lungs facilitate inhalation and exhalation. These intrinsic physiological processes influence the IBF continuously, which reflects the heat rate (HR) and respiration rate (RR), respectively. Hence, IBF signals existing within arteries contain informative data about these vital signs, such as HR and RR.

Extraction HR and RR from IBF signals. According to the frequency difference between HR and RR, we leverage different filters to select HR and RR signals from the IBF signals. Considering that the heartbeat rate of humans is usually between 60 and 100 bpm, we first pass the IBF signal through a band-pass filter of [0.6 Hz, 3 Hz] to remove the DC component and the high-frequency noise. We then leverage Fast Fourier Transform (FFT) to identify the periodicity which corresponds to the HR. Similarly, since adults breathe 12 to 20 times per minute, we use a band-pass filter of [0.2 Hz, 1 Hz] and adopt FFT to identify the RR.

2.2 Measuring IBF Signals with GMR Sensor

Although the variation of the induced biomagnetic field signal contains a wealth of vital sign information, the strength of this signal is extremely low (usually below 10^{-10} T [12]), making it challenging to be detected. As such, prior works proposed leveraging the giant magnetoresistance (GMR) unit, a highly sensitive magnetic sensor, to measure IBF signal variations.

GMR Sensor. GMR refers to the phenomenon in which the electrical resistivity of a magnetic material changes greatly when it has an external magnetic field as compared with the absence of an external magnetic field. There are two types of GMR units: parallel GMR and anti-parallel GMR, which means that the resistance is positively or negatively correlated with the strength of the external magnetic field.

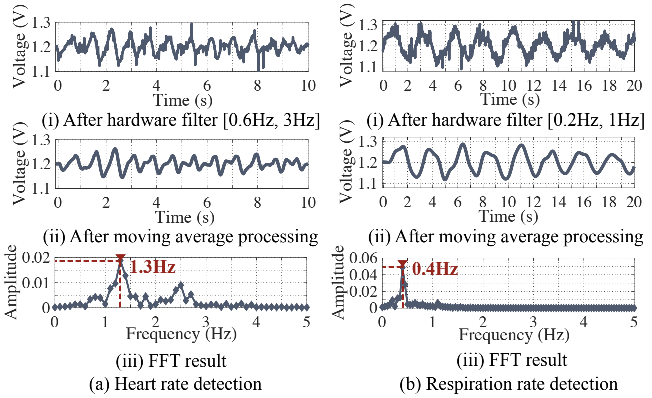

Fig. 4. Feasibility study result [9].

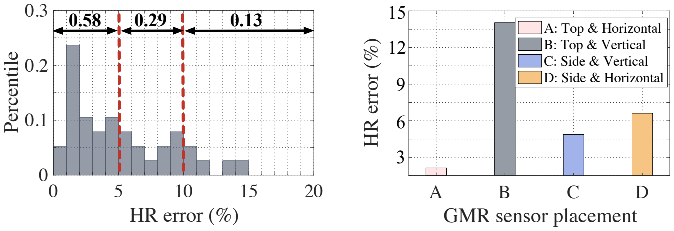

(a) Human diversity (b) Placement diversity

Fig. 5. Benchmark results demonstrate the impact of (a) human diversity and (b) placement diversity of GMR sensor on IBF signals detection [9].

A commodity GMR sensor consists of two parallel GMR units and two anti-parallel GMR units, which form a full Wheatstone bridge [13] to measure the subtle changes in the magnetic field. As shown in Figure 3, two parallel GMR units of bridge arms exhibit $R_{m1} = R + \Delta R(H)$, while the remaining two anti-parallel GMR units exhibit $R_{m2} = R - \Delta R(H)$. The output of this full-bridge GMR sensor is:

$$V_{out} = V_{in}(\frac{R_{m2}}{R_{m1}+R_{m2}} - \frac{R_{m1}}{R_{m1}+R_{m2}}) = V_{in}(\frac{\Delta R(H)}{R}) \quad (1)$$

where V_{in} is the bias voltage, R is the initial resistance of the GMR element, and $\Delta R(H)$ is the resistance variation caused by the external magnetic field (the induced biomagnetic field signal in our scenario). Note from the above equation that the GMR sensor exhibits a null output in the absence of an external magnet. Hence it offers an intrinsic compensation for thermal drift.

2.3 Understanding IBF-based Vital Sign Monitoring Through Benchmark Studies

Despite the existing research that explores the potential of utilizing IBF signals for human vital sign monitoring, numerous practical challenges still impede the practical implementation of this approach. In this section, we follow prior works [10], [7], [14], [8], [15] to develop a GMR-based IBF measurement testbed, and conduct a comprehensive benchmark study based on 30 volunteers. The goal is to understand the efficacy and limitations of this approach.

Experiment Setups. We use a 30 mT NdFeB disc permanent magnet with a diameter of 10 mm as the external magnet, to activate the blood flow and induce the IBF signals. Then we select a general-purpose NVE AA004 [16] GMR sensor to capture the IBF signals. The temperature compensation is achieved by the internal Wheatstone design of the GMR sensor. We place the permanent magnet on the radial artery of the wrist, and the GMR sensor is placed horizontally on top of the external magnet with

Authorized licensed use limited to: Zhejiang University. Downloaded on October 30,2024 at 06:35:33 UTC from IEEE Xplore. Restrictions apply.
© 2024 IEEE. Personal use is permitted, but republication/redistribution requires IEEE permission. See https://www.ieee.org/publications/rights/index.html for more information.

This article has been accepted for publication in IEEE Transactions on Mobile Computing. This is the author's version which has not been fully edited and content may change prior to final publication. Citation information: DOI 10.1109/TMC.2024.3452499

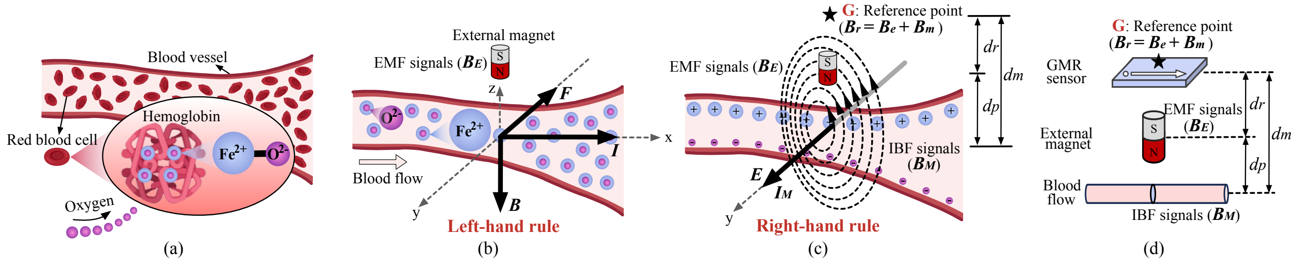

(a) (b) (c) (d)

Fig. 6. Detection theory of MagWear. (a) Structure of the arterial vessel. (b) The positive ions in the arterial vessel are subject to Lorentz forces when the external magnet is applied. (c) Under the influence of Lorentz force, positive and negative ions move towards both sides of the blood vessel, and generate induced current and induced biomagnetic field (IBF) signals. The IBF signals will further affect the magnetic flux at the reference point. (d) Model abstraction [9].

a distance of 10 mm. For the ground truth, volunteers wear an FDA-approved Fingertip Pulse Oximeter [17] on the index finger. **Signal Processing**. Considering that the heartbeat rate of humans is usually between 60 and 100 bpm [18], we first pass the signal output from the GMR sensor through a band-pass filter of $[0.6\,\text{Hz}, 3\,\text{Hz}]$ to remove the DC component and the high-frequency noise. Figure 4(a-i) shows the measured IBF signals from one of the 30 experiment participants. After that, a moving average processing is applied to remove circuit noise and signal burrs. As shown in Figure 4(a-ii), the filtered IBF signals present clearly periodic characteristics. We then leverage Fast Fourier Transform (FFT) to identify the periodicity which corresponds to the heartbeat rate (HR). As shown in Figure 4(a-iii), the measured heartbeat rate is about $1.3\,\text{Hz}$. The respiratory rate is obtained in a similar way. The output signals from the GMR sensor first pass through a band-pass filter of $[0.2\,\text{Hz}, 1\,\text{Hz}]$, since adults breathe 12 to 20 times per minute. Then we adopt FFT to identify the respiratory rate. As shown in Figure 4(b), the measured respiratory rate is about $0.4\,\text{Hz}$.

We have two key observations drawn from the experimental results shown in Figure 5.

- **Observation I: The vital sign monitoring accuracy varies significantly with different users.** Figure 5(a) presents the histogram of the errors of heart rate (HR) across all volunteers. The HR detection accuracy exhibits substantial variation among the 30 participants: 58% displayed commendable HR detection accuracy with errors between 0–5%; 29% had a marginally larger detection error, specifically in the 5% –10% range; and 13% showcased an even more pronounced error rate of 10% –16%. Based on the ANSI specified error criterion for cardiac monitors and HR meters [19], an error rate of 10% (or 5 bpm) is deemed significant, compromising the true reflection of a user's cardiac health.
- **Observation II: The placement of GMR sensor greatly impacts the vital sign monitoring accuracy.** As shown in Figure 5(b), the measured IBF signals exhibit different HR accuracy when the GMR sensor is placed in four different ways (position & orientation). Specifically, when the GMR sensor is positioned horizontally above the external magnet, the heart rate detection yields a minimal error of 1.48%. Conversely, placing the GMR sensor vertically atop the external magnet results in a substantial increase in heart rate detection error, reaching up to 13.8%. Similarly, the two alternative positions were tested, revealing a reduction in detection error to approximately 4.7% and 6.5%, respectively.

3 THEORETICAL ANALYSIS OF IBF

In this section, we build a mathematical model to understand IBF signal generation (§3.1). This model not only explains the disparities observed in vital sign monitoring effectiveness across various users but also provides valuable insights that influence the design considerations of MagWear (§3.2).

3.1 Modeling IBF Signal Generation

We model the relationship between the external magnetic field (EMF) signals and the induced biomagnetic field (IBF) signals, and then quantitatively analyze various factors that affect the IBF signals.

Inspired by the Hall effect [20], we added an external magnet over the blood vessel to generate the IBF signals. As shown in Figure 6(b), according to the left-hand rule, the charged particle (like Fe^{2+}) will feel Lorentz force F and it can be calculated by:

$$\boldsymbol{F} = q \cdot \boldsymbol{v} \times \boldsymbol{B} \tag{2}$$

where q is the charge of the particle, v is the speed of the particle, and B is the magnetic field strength felt by the particle.

Under the influence of the Lorentz force, charged particles continuously move in the direction of the Lorentz force and generate an electric field. As shown in Figure 6(c), when the Lorentz force and the electric field force reach equilibrium, we can obtain the following relationship:

$$q \cdot \boldsymbol{v} \times \boldsymbol{B} = \boldsymbol{E} \cdot q \tag{3}$$

where $\boldsymbol{E}$ is the electromotive force generated by the positive and negative particles, and we have $\boldsymbol{E} = \boldsymbol{v} \times \boldsymbol{B}$. The induced current $\boldsymbol{I_M}$ generated under this electric field is:

$$\boldsymbol{I_M} = \frac{\boldsymbol{E}}{R_0} = \frac{\boldsymbol{v} \times \boldsymbol{B}}{R_0} \tag{4}$$

where R_0 is the resistance of blood flow.

According to Ampère's right-hand rule, the induced current generates the IBF signals, and the strength of the IBF signals $\boldsymbol{B_M}$ is:

$$\boldsymbol{B_M} = \frac{\mu_0 \boldsymbol{I_M} \times \boldsymbol{e_r}}{2\pi r} = \frac{\mu_0 \boldsymbol{v} \times \boldsymbol{B} \times \boldsymbol{e_r}}{2\pi r R_0} \tag{5}$$

where μ_0 is the magnetic permeability, $\boldsymbol{e_r}$ is the vertical component of the current vector, and r represents the distance from the induced current.

Detecting the IBF signals. In practice, we detect the variation in IBF signals by measuring the magnetic field at a point above the blood vessel, *e.g.*, the reference point "G" shown in Figure 6(c) and Figure 6(d). Now let's assume the strength of the external magnet is $\boldsymbol{B_E}$, the distance from the external magnet to the reference point, from the external magnet to the blood vessel, and from the blood vessel to the reference point is d_r, d_p, and $d_m = (d_r + d_p)$, respectively. Then the EMF signals at the reference point "G" can be written as $\boldsymbol{B_e} = h\frac{\boldsymbol{B_E}}{{d_r}^3}$. Likewise, the IBF signals generated by the blood flow at the reference point "G" can be represented

Authorized licensed use limited to: Zhejiang University. Downloaded on October 30,2024 at 06:35:33 UTC from IEEE Xplore. Restrictions apply.

© 2024 IEEE. Personal use is permitted, but republication/redistribution requires IEEE permission. See https://www.ieee.org/publications/rights/index.html for more information.

This article has been accepted for publication in IEEE Transactions on Mobile Computing. This is the author's version which has not been fully edited and content may change prior to final publication. Citation information: DOI 10.1109/TMC.2024.3452499

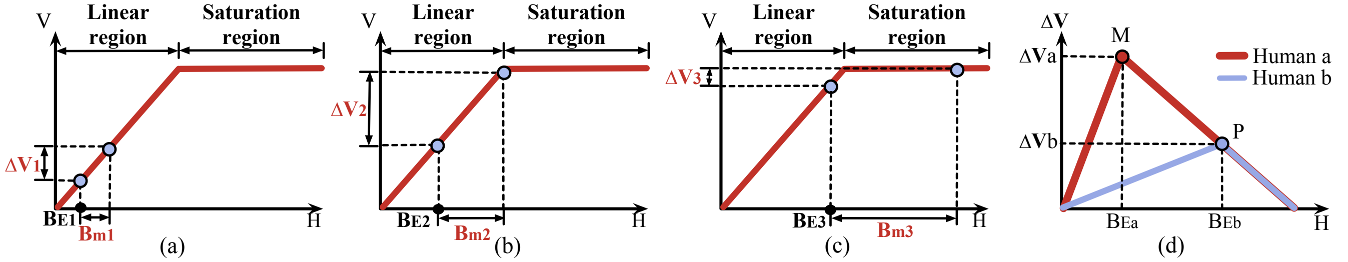

Fig. 7. (a–c) Output signal strength of the GMR sensor when applying different external magnetic fields; (d) The relationship between the GMR sensor's output amplitude and the external magnet strength [9].

as $\boldsymbol{B_m} = \frac{\mu_0 \boldsymbol{v}\times\boldsymbol{B}\times\boldsymbol{e_r}}{2\pi(d_r+d_p)R_0} = \frac{\mu_0 \boldsymbol{v}\times\boldsymbol{B_E}\times\boldsymbol{e_r}}{2\pi(d_r+d_p){d_p}^3R_0}$. Hence the overall magnetic field sensed by the GMR sensor at point "G" is:

$$\boldsymbol{B_r} = \boldsymbol{B_e} + \boldsymbol{B_m} = \underbrace{h\frac{\boldsymbol{B_E}}{{d_r}^3}}_{EMF\ signals} + \underbrace{\frac{\mu_0 \boldsymbol{v}\times\boldsymbol{B_E}\times\boldsymbol{e_r}}{2\pi(d_r+d_p){d_p}^3R_0}}_{IBF\ signals} \quad (6)$$

From the above equation, we have two observations.

- Firstly, the output of the GMR sensor reflects the variation of IBF signals since the EMF signals are constant under a fixed GMR sensor setup. This equation demonstrates the theoretical potential of utilizing IBF signal measurements for monitoring human vital signs.
- Secondly, this equation offers insights into the parametric factors that influence IBF signals, including the magnetic permeability μ_0, speed of particles v, the distance from the external magnet to the blood vessel d_p, and the resistance of the blood flow R_0, all of which are affected by human wrist size, fat thickness, and blood vessel dimensions. Accordingly, when applying the same measurement setup to different users, we are expected to get IBF signals in different SNRs. This essentially explains the variations we observed in the heart rate monitoring performance across different users (Figure 5).

3.2 Takeaways from the IBF Modeling

To ensure that MagWear can detect the heart rate accurately across different users, it's crucial to improve the SNR of IBF signals measured at each user. According to Equation 6, one feasible solution is to increase the intensity of the external magnetic field B_E by using a more potent external magnet. Whereas, how to find the best external magnetic field configuration for each individual? Blindly using a stronger magnet does not necessarily guarantee a higher heart rate monitoring accuracy as the magnetic field intensity may saturate the GMR sensor reading, resulting in an inferior monitoring accuracy.

Figure 7 explains this issue. Initially, when a low-intensity external magnetic field is applied (Figure 7(a)), the resultant induced biomagnetic field (IBF) signal would exhibit a low strength (as per Equation 6). Consequently, the variation $Bm1$ stemming from the heartbeat would be subtle, yielding a relatively minor GMR sensor reading ΔV_1. This scenario presents a significant hurdle to achieving accurate heart rate monitoring. As we gradually increase the intensity of the external magnetic field, the IBF signal strength also grows, which results in a more pronounced GMR sensor reading ΔV_2, as shown in Figure 7(b). In this case, we are expected to get a more accurate heart rate measurement. As the external magnetic field intensity is elevated even more (as depicted in Figure 7(c)), the potency of the induced IBF signal would exceed the GMR sensor's effective detection range, entering a saturation region where alterations in the GMR sensor reading cease despite escalating IBF signal strength. Consequently, the amplified fluctuation in the IBF signal ($Bm3$) caused by the heartbeat merely corresponds to a minimal change in GMR readings (ΔV_3), ultimately leading to suboptimal accuracy in monitoring heart rate.

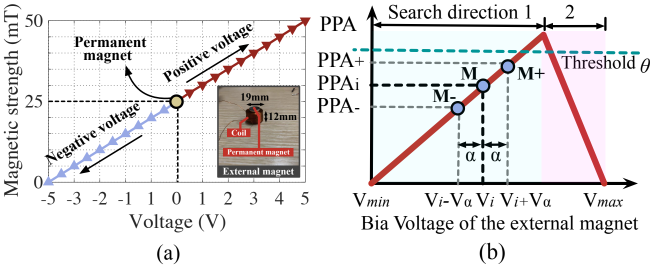

Fig. 8. External magnet strength. (b) The relationship between PPA and the bias voltage of the external magnet [9].

4 AUTOMATIC IBF SIGNAL TUNING

In this section, we present a software-hardware co-design approach that can automatically tune the IBF signal for each individual. We first describe the programmable external magnetic field design (§4.1) that allows us to freely change the intensity of the external magnetic field. We then present our online IBF signal tuning algorithm (§4.2).

4.1 Programmable External Magnetic Field

We build a programmable external magnetic field (EMF) module based on the electromagnetic induction phenomenon – when an electric current traverses a coil, it generates an encompassing magnetic field [21]. As shown in Figure 8(a), the programmable EMF module is constructed by overlaying an electromagnet of $[-25\ \text{mT}, 25\,\text{mT}]$ on a permanent magnet of $25\,\text{mT}$, thus generating an external magnetic field of $[0, 50\,\text{mT}]$. The external magnetic field is the superposition of the permanent magnet and the electromagnet. The permanent magnet provides a basic magnetic bias and the electromagnet is used to adjust the external magnetic strength.

4.2 Online IBF Signal Tuning Algorithm

In MagWear, we introduce a feedback-loop algorithm designed for tuning IBF signals. This online algorithm employs the past IBF signal reading (provided by the GMR sensor) as a reference to fine-tune the bias voltage of the electromagnet, aiming to maximize the SNR of the IBF reading.

We first characterize the SNR of the IBF signal readings. In particular, we choose **P**eak-**P**eak to **A**verage ratio (PPA) metric to characterize the quality of the received IBF signals. The PPA of an IBF signal is defined as the peak-to-peak intensity within $[0.6\,\text{Hz}, 3\,\text{Hz}]$ frequency band, where heartbeat signal stays, over

Authorized licensed use limited to: Zhejiang University. Downloaded on October 30,2024 at 06:35:33 UTC from IEEE Xplore. Restrictions apply.
© 2024 IEEE. Personal use is permitted, but republication/redistribution requires IEEE permission. See https://www.ieee.org/publications/rights/index.html for more information.

This article has been accepted for publication in IEEE Transactions on Mobile Computing. This is the author's version which has not been fully edited and content may change prior to final publication. Citation information: DOI 10.1109/TMC.2024.3452499

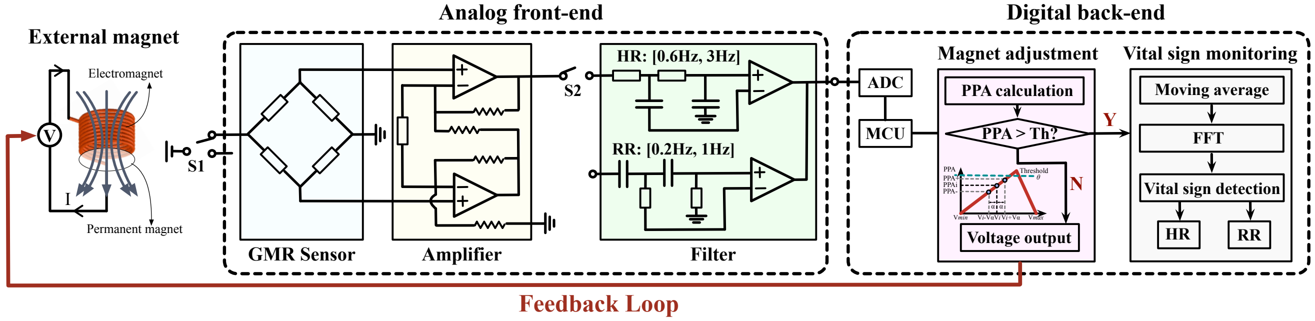

Fig. 9. The schematic of MagWear [9].

Algorithm 1: Online adaptive tuning algorithm

```
input : $V_{min}, V_{max}$ ;                       // voltage range
        $V_\alpha$ ;                                 // voltage tuning step length
        $N$ ;                                        // maximum search attempts
        $\theta \leftarrow \{4.7, 8.5, 11.2\}$ ;     // PPA thresholds
        $\theta_t \leftarrow 4.7; i \leftarrow 0$;
output: Feasible bias voltage $V_{out}$;
1  while $\theta_t$ is in $\theta$ and $i \le N$ do // initialization
2      $V_i \leftarrow \frac{V_{min}+V_{max}}{2}$;
3      $PPA_i \leftarrow$ CompPPA($V_i$);
4      if $PPA_i \le \theta_t$ then // decide search direction
5          $PPA_+ \leftarrow$ CompPPA($V_i + V_\alpha$);
6          $PPA_- \leftarrow$ CompPPA($V_i - V_\alpha$);
7          if $PPA_+ \ge PPA_-$ then // binary search
8              $V_{min} \leftarrow V_i$;
9              $V_i \leftarrow \frac{V_{min}+V_{max}}{2}$;
10             return $V_i$;
11         else
12             $V_{max} \leftarrow V_i$;
13             $V_i \leftarrow \frac{V_{min}+V_{max}}{2}$;
14             return $V_i$;
15     else
16         Update $\theta_t$; // update a tighter threshold
17     $i++$;
```

the average signal intensity within this band. Extensive results show that the error rate reduces to its minimum and becomes stable when the PPA exceeds 2%.

Algorithm 1 outlines the IBF signal tuning process. Our algorithm searches for the optimal bias voltage within a voltage range. Each time we compare the current PPA value with that corresponding to the intermediate voltage, then we reduce the search range by half until we find the optimal bias voltage. This process is similar to the binary search. Specifically, the function $CompPPA()$ is called to obtain the PPA of the received IBF signal in the current bias voltage input settings. Let the range $[V_{min}, V_{max}]$ denote the voltage limits of the electromagnet, which govern the boundaries for the magnetic strength value of B_E. The initial bias voltage of the electromagnet V_i is set to $(V_{min} + V_{max})/2$.

To expedite the search process, we leverage the monotonic properties of the PPA metric and adjust the acceptable HR threshold in response to user variations. Taking Figure 8(b) as a reference, if PPA_i of the received IBF signal is less than a PPA threshold θ, the algorithm updates the bias voltage to $(V_i + V_\alpha)$ and $(V_i - V_\alpha)$ and gets two PPA readings, namely PPA_+ and PPA_-, based on these two bias voltage settings. V_α is the voltage tuning step length and it can be dynamic. The step size decreases as the PPA value approaches the maximum value. These two PPA values essentially discern the slope's direction of the PPA curve (*i.e.*, point M_+ and M_-). After identifying the direction (by comparing PPA_+ with PPA_-), the algorithm runs a binary search (lines 4−14) to narrow down the search space, expediting the searching. The binary search is lightweight and can run on a microcontroller efficiently. The initial PPA threshold θ is empirically set to 4.7. It grows whenever the searched result meets the HR error limits.

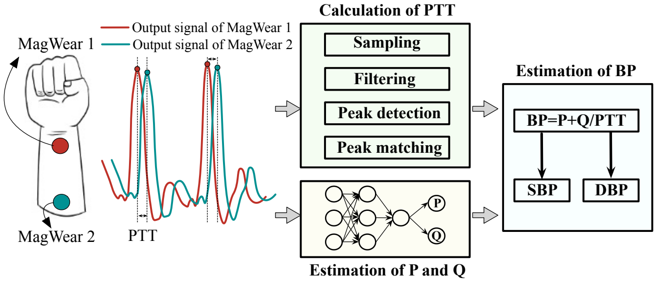

Fig. 10. The schematic of blood pressure.

5 EXTENDING TO BLOOD PRESSURE ESTIMATION

5.1 Basic Idea

Detection theory. Pulse Wave Velocity (PWV), defined as the velocity of the arterial pulse through the cardiovascular system, can be used as a good estimator of BP, as proven in some references [22], [23]. Usually, PWV can be calculated as a division of distance between pulse acquisition sites by Pulse Transition Time (PTT). We can further leverage the following equation to estimate the BP:

$$BP = P + \frac{Q}{PTT} \tag{7}$$

where P and Q are two parameters.

Both the systolic blood pressure (SBP) and diastolic blood pressure (DBP) can be estimated by the above Eq. 7 with different parameters of P and Q. In other word, the SBP and DBP satisfy the following relationship:

$$BP_S = P_S + \frac{Q_S}{PTT} \tag{8}$$

$$BP_D = P_D + \frac{Q_D}{PTT} \tag{9}$$

when given PTT, the key to SBP (BP_S) calculation is to estimate the parameters of P_S and Q_S. Similarly, the key of DBP (BP_D) calculation is to estimate the parameters of P_D and Q_D.

Feasibility exploration. In this paper, we leverage PTT to achieve the BP estimation. Figure 10 shows the BP detection process and Figure 9 shows the schematic of MagWear to obtain the heartbeat signals. We place the MagWear devices in two different positions along the arm. The readings of the GMR sensors in these two positions are similar but differ in phase. The phase difference is used to estimate the PTT. We conduct experiments to observe the PTT variation when we change the distance between two MagWear devices from 5cm to 12cm. The experiment setting

Authorized licensed use limited to: Zhejiang University. Downloaded on October 30,2024 at 06:35:33 UTC from IEEE Xplore. Restrictions apply.
© 2024 IEEE. Personal use is permitted, but republication/redistribution requires IEEE permission. See https://www.ieee.org/publications/rights/index.html for more information.

This article has been accepted for publication in IEEE Transactions on Mobile Computing. This is the author's version which has not been fully edited and content may change prior to final publication. Citation information: DOI 10.1109/TMC.2024.3452499

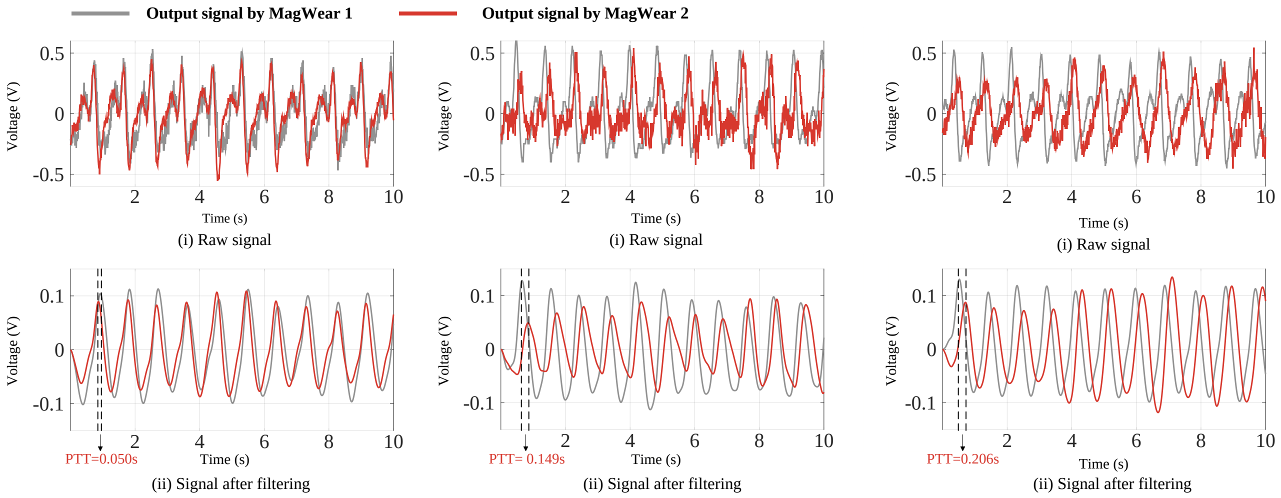

(a) 5cm (b) 10cm (c) 12cm

Fig. 11. The output of GMR sensors in different places (a) 5cm (b) 10cm (c) 12cm.

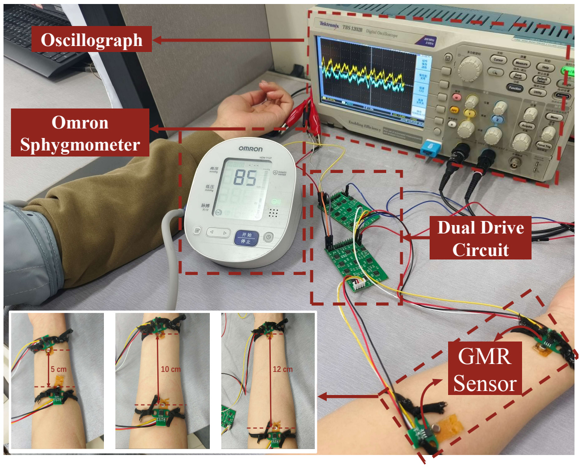

Fig. 12. The experiment setup of blood pressure estimation.

is shown in Figure 12. As shown in Figure 11, we find that the average PTT at the distances of 5cm, 10cm, and 12cm are 0.050s, 0.149s, and 0.206s, respectively. The larger the distance between MagWear devices, the larger the PTT, but the higher the deployment cost. Taking into account both PTT and deployment cost, we choose the MagWear devices distance as 10cm. The above experiments demonstrate the feasibility of BP estimation by using the PTT.

5.2 Blood Pressure Estimation

In this subsection, We introduce the specific BP estimation method, including the calculation of PTT, estimation of P and Q, and estimation of BP.

5.2.1 Calculation of PTT

During the process of calculating PTT from the GMR sensor readings, there are several challenges. First, the heart rate signal exhibits different waveforms due to varying states of the heart, such as R-waves, P-waves, and T-waves, all resembling peak points. While the time interval between two R-waves is typically measured in PTT, other wave signals may produce false positive peaks, impacting the accuracy of PTT calculation. Second, discrepancies in time offset or relative movement between two GMR sensor readings could result in unmatched peak points. These inaccuracies in PTT calculation can affect BP estimation. In this way, we propose a specific PTT calculation method to eliminate these errors.

Sampling and normalization. We set the sliding window size to 10s and the sampling rate to 100Hz to obtain enough raw data. Then, the data is normalized to avoid inconsistencies in the signal strengths of the two GMR sensors.

Low-pass filtering. After sampling the GMR sensor output signals, there are still small spurious signals, and these signals produce many false positive points when detected by the local maximum peak. To make the waveform as smooth as possible, a further digital low-pass filter is applied to the waveform. To maximize the suppression of clutter signals in the heart rate frequency range, we chose a low-pass filter with a cut-off frequency of 0.7Hz.

Peak detection with a threshold. First, we obtain all peak points by local maximum detection. Then, considering that the peak value of the R-wave is much larger than the peaks of the other waves, we remove the false positive peaks generated by other waves by averaging the threshold detection. Through experimental analysis, the threshold was generally chosen to be 0.7× of the average threshold.

Peak matching between two sequences. In the experiment, there are instances where certain peak locations of the two signals do not align perfectly. This discrepancy is caused by the temporal offset between two GMR sequences or errors caused by the relative movement. To address this issue, we employ a dynamic programming (DP) algorithm to achieve sequence matching.

Our key observation is that the timing error resulting from signal offset or relative movement error between the two sensors is more higher than that of the PTT by a factor of ten. Therefore, we can group the peak points to minimize the overall time difference in the matching process. To be specific, for the first and second output signals of GMR sensors, the time of the peak point can be denoted as $seq1 = \{a_1, a_2, ..., a_m\}$ and $seq2 = \{b_1, b_2, ..., b_n\}$, respectively. n is not equal to the m. We define the Euclidean distance as

$$d(a_i, b_j) = \sqrt{(a_i - b_i)^2} \tag{10}$$

Our optimization objective is to minimize the sum of the

Authorized licensed use limited to: Zhejiang University. Downloaded on October 30,2024 at 06:35:33 UTC from IEEE Xplore. Restrictions apply.
© 2024 IEEE. Personal use is permitted, but republication/redistribution requires IEEE permission. See https://www.ieee.org/publications/rights/index.html for more information.

This article has been accepted for publication in IEEE Transactions on Mobile Computing. This is the author's version which has not been fully edited and content may change prior to final publication. Citation information: DOI 10.1109/TMC.2024.3452499

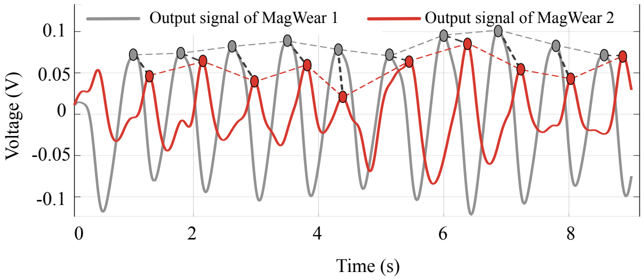

Fig. 13. The result of peak matching.

Euclidean distances of all peak pairs:

$$\min_{i_k, j_k} \sum_{k=1}^{\min(m,n)} d\left(a_{i_k}, b_{j_k}\right) \tag{11}$$

where i_k and j_k represent the indexes of the elements in the $seq1$ and $seq2$ in the k-th set of matched pairs, respectively, and i_k and j_k are unique.

The DP algorithm for sequence matching is as follows. First, we define C_{ij} as the cost matrix and D_{ij} as the cumulative cost matrix. C_{ij} represents the cost of aligning the i-th element of $seq1$ with the j-th element of $seq2$. D_{ij} represents the minimum cumulative cost to align the prefix of $seq1$ ending at position i with the prefix of $seq2$ ending at position j. The state transfer equation can be represented as

$$D_{ij} = C_{ij} + \min(D_{i-1,j}, D_{i,j-1}, D_{i-1,j-1}) \tag{12}$$

Finally, the best grouping is obtained based on the cumulative cost matrix, as shown in Figure 13.

PTT Averaging. Within a sliding window, the sequence-matching algorithm is able to obtain multiple sets of well-matched peak points. One PTT can be obtained for each set of peak peaks. therefore we use the mean PPT to characterize the overall PTT of this window.

5.2.2 Estimation of P and Q

We leverage a learning-based approach[24] to estimate the parameters of P and Q.

Network architecture. We utilize two GMR sensor output signals as inputs. Before entering the network, these signals undergo pre-processing operations including normalization and filtering. To extract deeper features, we employ two parallel branches for temporal and spectral feature extraction following reshaping operations. The network structure is shown in Figure 14. The first branch focuses on time series feature extraction. It comprises four consecutive residual blocks, each containing three convolutional layers. Each convolutional layer is followed by a batch normalization (BN) layer for normalization and an activation layer to expedite model convergence. Additionally, residual connections are utilized to accelerate model convergence. The second branch is dedicated to spectral feature extraction. This module generates spectrograms via short-time Fourier transform (STFT) and employs a GRU unit to capture time-dependent information from the spectrogram. Subsequently, the feature information obtained from the first branch is aggregated, and further fine-grained time-dependent features are extracted by the GRU unit. Similarly, the feature information from the second branch is concatenated to extract spectral-related features. Finally, after concatenating all fine-grained features, two parameters, P and Q, are predicted using a dense layer.

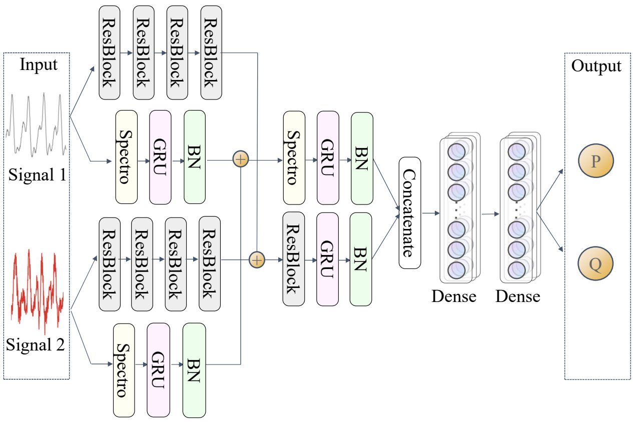

Fig. 14. The DNN-based structure to estimate parameters of P and Q.

Loss function. The method we employ is a fully supervised learning approach. During training, the network outputs estimated values for P and Q. Subsequently, a BP value is computed using Equation 7. We then utilize the minimum mean square error as a loss function to quantify the disparity between the estimated BP and the actual BP.

$$\text{Loss} = \frac{1}{n} \sum_{i=1}^{n} (\text{BP}_i - \hat{\text{BP}}_i)^2 \tag{13}$$

where n denotes the number of batch size, BP and $\hat{\text{BP}}$ denotes the ground truth and estimated BP, respectively. The learning rate of the training model is 1e-4, the batch size is 256 and the maximum number of training rounds is 50.

6 IMPLEMENTATION

We prototype MagWear on a two-layer printed circuit board (PCB) using COTS analog components and an ultra-low power ESP32 MCU [25]. Figure 9 and Figure 15 show the hardware schematic and the hardware prototype. MagWear consists of three parts: (1) external magnet, (2) analog front-end, and (3) digital back-end. The prototype costs approximately \$15.3 USD.

- **External magnet.** The external magnet is built by overlaying an electromagnet of $[-25\,\text{mT}, 25\,\text{mT}]$, a pure copper coil with 400 turns, on a permanent magnet of $25\,\text{mT}$. The size of the external magnet is $19\,\text{mm} \times 12\,\text{mm}$.
- **Analog front-end.** We adopt NVE AA004 [16] GMR sensor to detect IBF signals. The output of the GMR sensor is connected to a low-power amplifier composed of INA126 [26] with an amplification gain of 800. With this setting, the variation of the IBF can be captured and amplified. The output signal from the amplifier is further sent to the filtering processing circuit. There are four different low-pass filters composed by OP07 [27] from Texas Instruments, and their cutoff frequencies are $0.2\,\text{Hz}$, $0.6\,\text{Hz}$, $1\,\text{Hz}$, and $3\,\text{Hz}$. By cascading these low-pass filters, two different bandpass filters $[0.6\,\text{Hz}, 3\,\text{Hz}]$ and $[0.2\,\text{Hz}, 1\,\text{Hz}]$ can be formed to filter out the desired heartbeat signals and respiratory signals, respectively. Then the filtered analog signals are shifted to 0-5V by a voltage converter[1] and are forwarded to the digital back-end. There are two switches, where "S_1" enables MagWear to enter working mode and "S_2" is used to select the suitable filter. When measuring the blood pressure, we place the MagWear front-ends at two different positions (Wrist and elbow) and then select the frequency of the filter as $[0.6\,\text{Hz}, 3\,\text{Hz}]$. Finally, we calculate the

---

[1] ADC can only sample positive voltage signals.

Authorized licensed use limited to: Zhejiang University. Downloaded on October 30,2024 at 06:35:33 UTC from IEEE Xplore. Restrictions apply.
© 2024 IEEE. Personal use is permitted, but republication/redistribution requires IEEE permission. See https://www.ieee.org/publications/rights/index.html for more information.

This article has been accepted for publication in IEEE Transactions on Mobile Computing. This is the author's version which has not been fully edited and content may change prior to final publication. Citation information: DOI 10.1109/TMC.2024.3452499

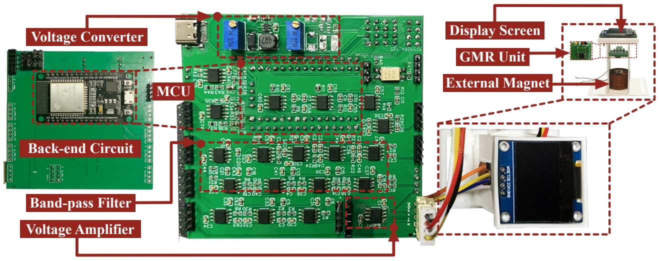

Fig. 15. The prototype of MagWear and experiment setup [9].

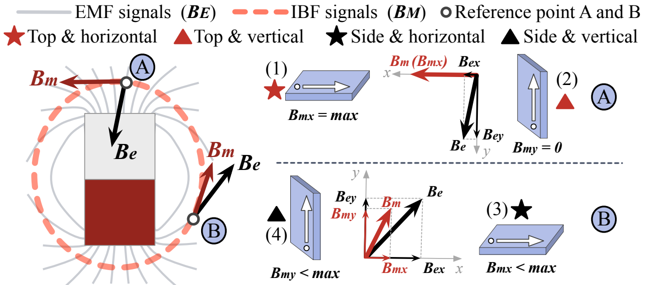

Fig. 16. The impact of the placement of GMR sensor.

time difference based on the phase difference of the IBF signals obtained from two MagWear front-end.

- **Digital back-end.** We adopt a 12-bit ADC with a sampling rate of 100 Hz to digitalize these analog signals and send these data to the ESP32 [25] MCU. The MCU is responsible for (a) magnet adjustment: dynamically controlling the bias voltage of the electromagnet via a driver OPA549 [28]; (b) vital sign monitoring: measuring HR, RR, and BP after signal processing.
- **Placement of the GMR Sensor.** We carefully understand the impact of GMR sensor's placement (position & orientation) on the detection result of MagWear, as elaborated in Figure 16: (1) Top & horizontal : Both the EMF signals and the IBF signals only have the horizontal component. Thus the output voltage of the GMR sensor has a good SNR and exhibits clearly distinguishable signal features. (2) Top & vertical: There is almost no signal component of IBF in the vertical direction. (3/4) Side & horizontal and side & vertical: Both the EMF signals and the IBF signals have horizontal and vertical components. However, the decomposition of IBF signals in two directions will affect the response sensitivity of the GMR sensor. The experimental result in Figure 5(b) is consistent with our above analysis. Hence, we place the GMR sensor horizontally on the top of the external magnet to maximize its detection sensitivity.
- **Magnet safety.** Ensuring user safety in the presence of magnetic fields is paramount. The Magnet Safety Guideline from ACGIH dictates that a magnetic field strength of up to 60mT is deemed safe for whole-body exposure, while the extremities can tolerate up to 600mT [29], [30]. Our measurements show that the most potent magnet in MagWear generates a magnetic field strength of less than 50mT at a distance of 1cm. This is safe for everyday use and notably falls well under the advised safety limits. Certain individuals, especially those with cardiac implants, should exercise extra caution. Their safe exposure limit is much lower, capped at 0.5mT. We strongly advise such individuals to seek counsel from their healthcare providers before using the device [31].
- **Device miniaturization.** MagWear has miniaturized its form factor shown in Figure 17: 1) We integrate the analog front-end and the digital back-end on one PCB board to minimize the form factor as 38mm×45mm; (2) We adopt a flexible PCB design to compact the circuitry.

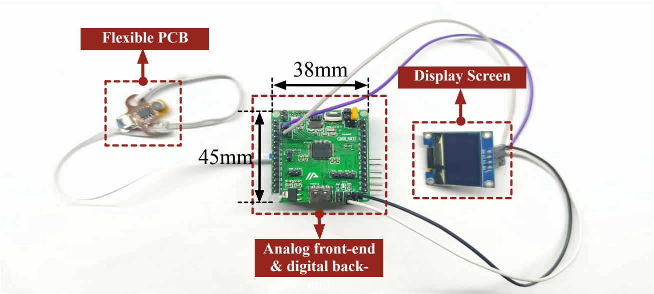

Fig. 17. MagWear miniaturization.

7 EVALUATION

7.1 Experiments Setup

Data collection and demographic information of the dataset. We recruit a total of 30 volunteers and the participant distribution is as follows. (1) The gender distribution is 20 males and 10 females, respectively. (2) 30 participants were divided into four groups based on age distribution. There are 8, 8, 7, and 7 volunteers respectively in the age group 20-30, 30-40, 40-50, and 50-60. (3) Based on the Body Mass Index (BMI), 30 participants were divided into four groups based on age distribution. There are 5, 10, 10, and 5 volunteers respectively in the age group 20-30, 30-40, 40-50, 50-60. We divide 30 participants into four groups, namely, underweight (BMI≤18.4), healthy (18.5≤BMI≤24.9), overweight (25.0≤BMI≤29.9), and obese (BMI≥30.0). (4) Each volunteer is asked to self-identify their skin tone. 13 out of 30 participants chose a skin tone rating of 1-3, 12 participants opted for 4-6, and 5 participants selected 7-10 on the scale. In addition, our IRB doesn't mandate specific quotas for recruiting participants and our recruitment process is open to all volunteers. Although we haven't covered the balanced representation of the sample, we hold confidence that our findings will generalize to a more diverse and expansive population. As shown in Figure 15, the volunteers wear MagWear in a way they feel comfortable. The ground truth is obtained by an FDA-approved device, LEPU PO6 Fingertip Pulse Oximeter [17]. Our testing protocol involves each user undergoing 5-minute assessments repeated 10 times.

Evaluation metrics. We adopt the following metrics to evaluate the performance of MagWear.

(i) *Mean Absolute Error (MAE)* is the mean absolute difference between the estimated value (denoted by V^E) and the ground truth (denoted by V^T) *i.e.*, $MAE = \frac{1}{N}\sum_{i=1}^{N}|V_i^E - V_i^T|$.

(ii) *Mean Percentage Error (MPE)* is the mean percentage difference between V^E and V^A, *i.e.*, $MPE = \frac{1}{N}\sum_{i=1}^{N}\frac{|V_i^E - V_i^T|}{V_i^T}$.

(iii) *Bland-Altman Diagram* analyzes the agreement between two measurement methods. It evaluates a bias between the mean differences and estimates an agreement interval.

Exclusion and inclusion factor. The exclusion and inclusion factor is the impact of skin tone. PPG measurements can sometimes be affected by variations in skin tone, as they rely on light absorption and reflection. IBF signals are less sensitive to these variations, potentially making them more reliable across a wider range of individuals. Given classical PPG's sensitivity to skin tone, our primary goal is to understand the inclusiveness of MagWear to the specific study population.

Authorized licensed use limited to: Zhejiang University. Downloaded on October 30,2024 at 06:35:33 UTC from IEEE Xplore. Restrictions apply.
© 2024 IEEE. Personal use is permitted, but republication/redistribution requires IEEE permission. See https://www.ieee.org/publications/rights/index.html for more information.

This article has been accepted for publication in IEEE Transactions on Mobile Computing. This is the author's version which has not been fully edited and content may change prior to final publication. Citation information: DOI 10.1109/TMC.2024.3452499

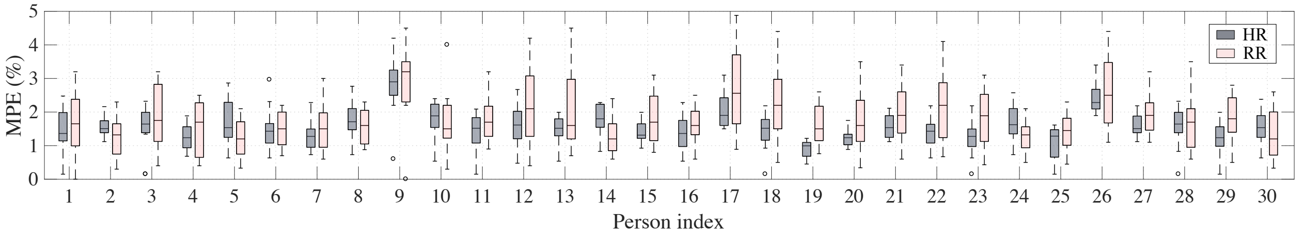

Fig. 18. Overall performance of HR and RR [9].

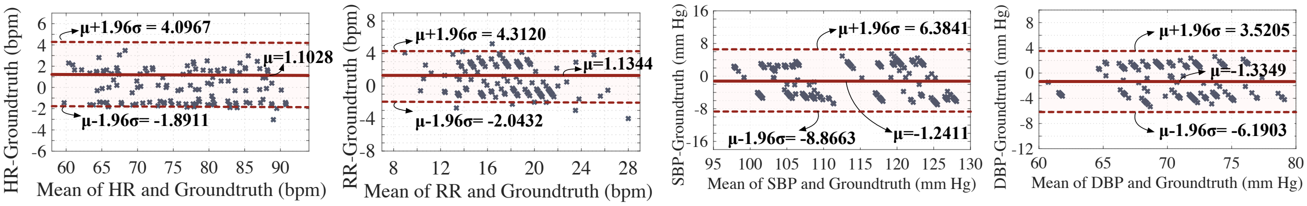

(a) HR (b) RR (c) SBP (d) DBP

Fig. 19. Bland-Altman diagram of MagWear's estimation results in HR, RR, SBP, and DBP.

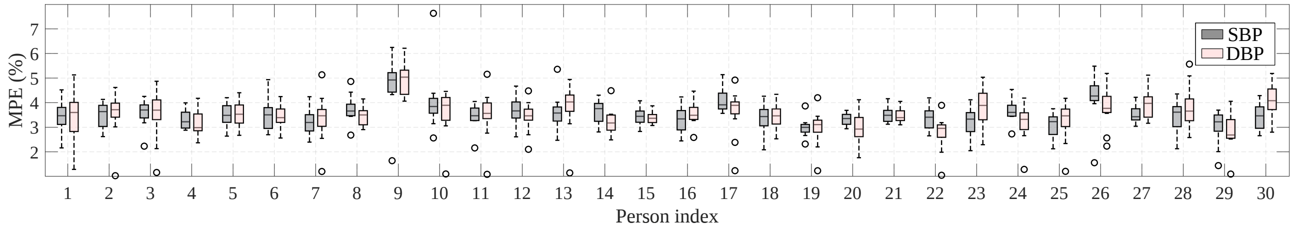

Fig. 20. Overall performance of SBP and DBP.

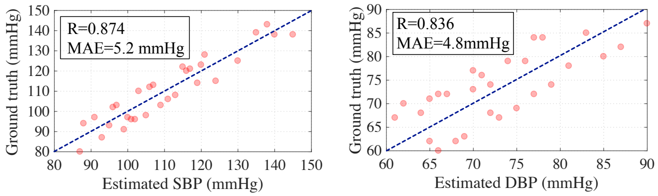

(a) SBP (b) DBP

Fig. 21. The correlation analysis of SBP and DBP.

7.2 Field Study

HR monitoring result. We first examined the HR monitoring accuracy among 30 volunteers. The results are summarized in Figure 18. Overall, MagWear achieves decent performance across all 30 participants, with a mean MPE at 1.55% for HR. We find that subjects 9, 17, and 26 have relatively higher MPE (>2%) than the remaining subjects. This could likely be attributed to the fact that these individuals tend to have higher body weights. Additionally, external magnetic fields might not readily stimulate and attenuate following encounters with bodily factors. We further leverage the Bland-Altman diagram to evaluate the agreement between the HR measured with MagWear and the ground truth, as shown in Figure 19(a). The mean and standard deviation of HR are 1.10% and 1.53%. It is clear that the bias between the two methods is limited with very low mean and narrow limits of agreement (red lines). Notably, the majority of the data points fall within the limits of agreement, denoting the two methods are in agreement.

RR monitoring result. We then examined the RR monitoring accuracy among 30 volunteers. Figure 18 shows the performance of MagWear. We observe a mean MPE at 1.79% for RR across all 30 participants. Figure 19(b) shows the Bland-Altman diagram to evaluate the agreement of RR measured with MagWear and the ground truth. The mean and standard deviation of RR are 1.13% and 1.62%.

BP monitoring result. We first examined the HR, RR, and BP monitoring accuracy, including the SBP and the DBP. The results are shown in Figure 20. Overall, MagWear achieves decent performance across all 30 participants, with a mean MPE at 3.35% for SBP and 3.89% for DBP, respectively. We find that subject 9 has a relatively higher MPE (>5%) than the remaining subjects. The reason behind this may be due to the fact that this individual tends to have a higher body weight. We further leverage the Bland-Altman diagram to evaluate the agreement between the SBP and DBP measured with MagWear and the ground truth, as shown in Figure 19(c) and Figure 19(d). Consequently, the mean and standard deviation of SBP are 1.24% and 3.89%, the mean and standard deviation of DBP are 1.33% and 2.47%. The result demonstrates that our method of MagWear and the ground truth of Omron Sphygmometer are in agreement.

Correlation analysis. We conduct correlation analysis for the blood pressure estimation across 30 volunteers. The result is shown in Figure 21. We observe the correlation coefficient of SBP and DBP is 0.874 and 0.836, respectively. The correlation analysis proves a good linear fit for blood pressure estimation.

7.3 Benchmark Study

Impact of age. We examine the impact of the user's age to verify MagWear's robustness. 30 volunteers of different ages wear MagWear and iWatch to detect HR. The result is shown in Figure 22(a). We have the following observation. MagWear and iWatch present similar MAE errors. The MAE of MagWear and iWatch vary from 1.24 bpm to 1.44 bpm and from 1.12 bpm to 1.31 bpm, respectively. In addition, the age group spanning 50-60 years exhibits a relatively higher MAE.

Impact of BMIs. We then compare the impact of different BMIs on MagWear 's and iWatch performance. We divide 30 participants into four groups, namely, underweight (BMI≤18.4), healthy (18.5≤BMI≤24.9), overweight (25.0≤BMI≤29.9), and obese (BMI≥30.0). As shown in Figure 22(b), iWatch achieves

Authorized licensed use limited to: Zhejiang University. Downloaded on October 30,2024 at 06:35:33 UTC from IEEE Xplore. Restrictions apply.
© 2024 IEEE. Personal use is permitted, but republication/redistribution requires IEEE permission. See https://www.ieee.org/publications/rights/index.html for more information.

This article has been accepted for publication in IEEE Transactions on Mobile Computing. This is the author's version which has not been fully edited and content may change prior to final publication. Citation information: DOI 10.1109/TMC.2024.3452499

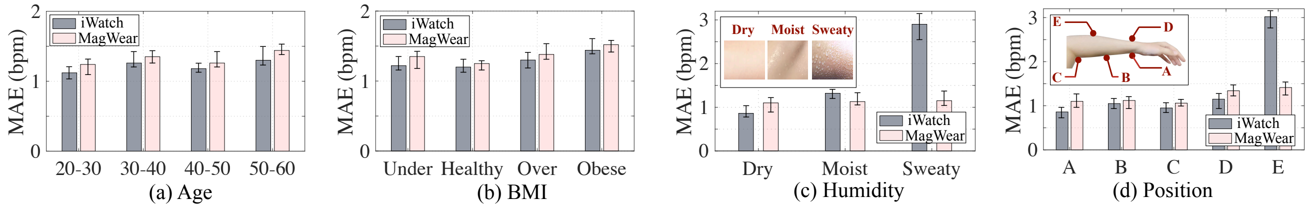

(a) Age (b) BMI (c) Humidity (d) Position

Fig. 22. MagWear performance under different settings of (a) age, (b) BMI, (c) humidity, (d) wearing position.

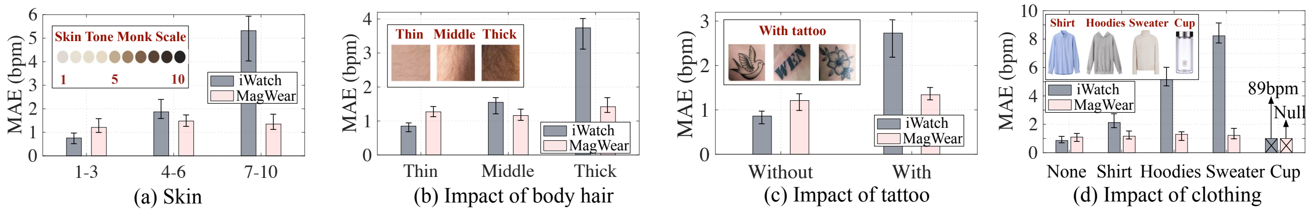

(a) Skin (b) Impact of body hair (c) Impact of tattoo (d) Impact of clothing

Fig. 23. MagWear performance under different settings of (a) skin tone, (b) body hair, (c) tattoo, (d) clothing [9].

MAE of 1.22 bpm, 1.20 bpm, 1.31 bpm, 1.44 bpm for four groups, and MagWear achieves MAE of 1.35 bpm, 1.25 bpm, 1.38 bpm, 1.52 bpm. We find that the MPE of MagWear and iWatch is relatively higher for obese subjects.

Impact of skin conditions. Given classical PPG's sensitivity to skin tone, our primary goal is to understand the inclusiveness of MagWear to the specific study population. The participant distribution is as follows: 13 out of 30 participants chose a skin tone rating of 1-3, 12 participants opted for 4-6, and 5 participants selected 7-10 on the scale. Although we haven't covered the entire Monk scale, we hold confidence that our findings will generalize to a more diverse population. The outcomes are presented in Figure 23(a). Notably, MagWear consistently achieves low MAEs ranging from 1.21% to 1.48% across all three skin tone groups, underscoring its inclusiveness across different skin tones.

Impact of body hair. Next, we evaluate the impact of body hair (Figure 23(b)). As the thickness of body hair increases, the MAE of iWatch grows by 4.4× from 0.85% to 3.74%, while the MAE of MagWear is relatively stable at 1.27%–1.42%. This is expected since compared to magnetic signals, optical signals are more susceptible to the occlusion of the body hair.

Impact of tattoo. Tattoos affect the propagation of optical signals. As shown in Figure 23(c), the MAE of iWatch with tattoo grows up to 2.73%, 2.04× higher than that of MagWear.

Impact of clothing. We then evaluate the impact of clothing to verify the non-contact characteristic of MagWear. Volunteers wear different clothes and then wear MagWear and iWatch on their wrists. The result is shown in Figure 23(d). As the thickness of the clothes increases, the MAE of MagWear grows by 1.1× from 1.10 bpm to 1.22 bpm, the MAE of iWatch grows by 9.56× from 0.86 bpm to 8.23 bpm. Note that the magnetic flux can penetrate through the clothing, the detection result of MagWear is more reliable and sensitive than that of iWatch. In contrast, clothing obstructs the optical path between the PPG sensor and blood flow, causing the HR measurements obtained by the iWatch through clothing to effectively represent blind estimations. Remarkably, we have found that the iWatch can still yield results when placed against objects, such as a cup.

Impact of humidity. We conduct tests when volunteers have different degrees of humidity on their arms. The evaluation result is shown in Figure 22(c). We find that MagWear is more resilient to humidity than iWatch. When varying from dry to sweaty, the MAE of MagWear varies from 1.06 bpm to 1.22 bpm, while the MAE of iWatch grows by 3.14× from 0.91 bpm to 2.86 bpm. This is because the presence of moisture affects the optical path significantly more than the magnetic path. Consequently, it's noteworthy that Apple cautions that water could impede heart-rate measurements when swimming.

Impact of wearing position. We conduct experiments to examine the impact of wearing position on the human body to verify MagWear's robustness. The volunteers wear MagWear and iWatch at different positions on the arm to detect HR. The various wearing positions and their corresponding outcomes are illustrated in Figure 22(d). We have the following two observations. First, the MAE varies with the wearing position. The MAE differences of MagWear and iWatch wearing at the best position ("A") and the worst position ("E") are 0.24 bpm and 1.61 bpm, respectively. Second, wearing position has less impact on MagWear than iWatch. For example, the MAE of MagWear is 2.14× less than that of iWatch at position "E", which is probably due to their different detection principles. iWatch adopts a PPG-based detection method and the bone at the position will affect most of the optical path, resulting in serious errors. MagWear adopts GMR-based detection method and the induced magnetic field can effectively penetrate bones, thus maintaining a lower MAE.

One-hour continuous study. We invite a participant with a darker skin tone to wear MagWear for an hour in daily activities, comprising periods of napping, sitting, and standing. The result is shown in Figure 24(a). We can find that the MAE of MagWear is more stable than that of iWatch, which means that MagWear exhibits relatively stable characteristics in long-term measurements. Furthermore, during the transition phases between different activities, both MagWear and the iWatch experience brief upticks in MAE. This can be attributed to the readjustment required as the subject transitions between distinct physiological states.

Impact of electromagnetic interference. The result is shown in Figure 24(b–d). (1) We measure the HR in the open playground and the fifth-floor laboratory to observe the impact of the earth magnetic field variation. We observe that the performance of MagWear on different locations is similar. This is expected since that the earth magnetic field declines exponentially with distance. In this way, the subtle earth magnetic field variation will not cause a significant change in the GMR sensor readings. (2) We conduct experiments to evaluate the impact of electromagnetic interference on MagWear. We place the MagWear next to a smartphone, WiFi AP, electric fan, and microwave oven. We have the following observations. Firstly, MagWear's MAE in the presence of interference is more compromised around the microwave oven than around the smartphone, WiFi AP, and electric fan. The MAE values for MagWear are measured at 14.1 bpm, 7.6 bpm,

Authorized licensed use limited to: Zhejiang University. Downloaded on October 30,2024 at 06:35:33 UTC from IEEE Xplore. Restrictions apply.
© 2024 IEEE. Personal use is permitted, but republication/redistribution requires IEEE permission. See https://www.ieee.org/publications/rights/index.html for more information.

This article has been accepted for publication in IEEE Transactions on Mobile Computing. This is the author's version which has not been fully edited and content may change prior to final publication. Citation information: DOI 10.1109/TMC.2024.3452499

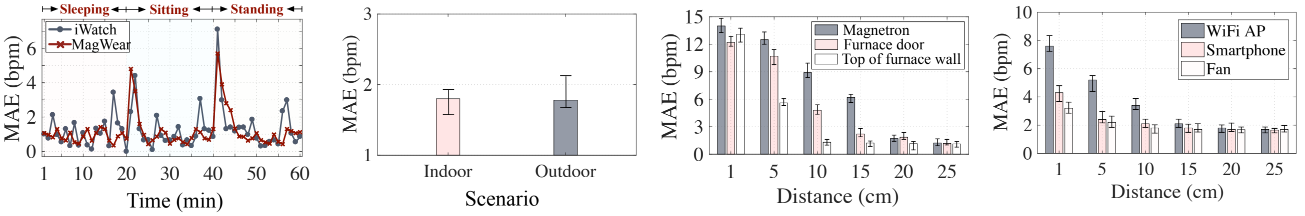

(a) One-hour continuous study (b) Impact of earth magnetic field (c) Impact of microwave oven (d) Impact of router, phone, and fan

Fig. 24. (a) One-hour study on a person. (b) Impact of electromagnetic interference.

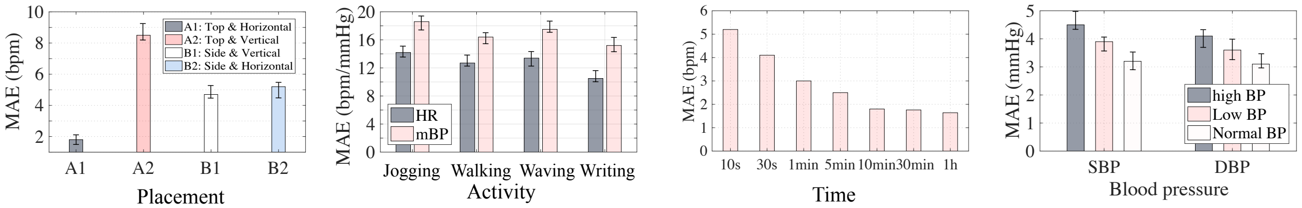

(a) Placement (b) Human motion (c) Exercise (d) Different individuals

Fig. 25. The impact of (a) device placement, (b) human motion, (c) exercise, and (d) different individuals on MagWear.

4.3 bpm, and 3.1 bpm when positioned at a distance of 1 cm from the microwave oven (magnetron), WiFi AP, smartphone, and electric fan. Secondly, the MAE decreases as the distance from the interference source increases. As the separation grows to 20 cm, the MAE values around the microwave oven (magnetron), WiFi AP, smartphone, and electric fan are lower than 2 bpm.

Impact of device placement. The placement of device (position & orientation) can affect the performance of MagWear. The result is shown in Figure 25(a). The measured MAEs are different when the GMR sensor is placed in four different ways (position & orientation). When the GMR sensor is positioned horizontally above the external magnet, the heart rate detection yields a MAE of 1.8 bpm. Hence, we place the GMR sensor horizontally on the top of the external magnet to maximize its detection sensitivity.

Impact of human motion. We conduct experiments to evaluate MagWear's performance under human mobility. We invite a participant to wear MagWear and perform four different activities (jogging, walking, waving, writing) when measuring heart rate (HR) and mean blood pressure (mBP). The experimental result is shown in Figure 25(b). The MAE of HR measurement is 14.2 bpm, 12.7 bpm, 13.4 bpm, 10.5 bpm. The MAE for mBP estimation is 18.6 mmHg, 15.7 mmHg, 13.2 mmHg, and 12.5 mmHg across these four activities. The MAE of MagWear in mobility is larger than that in stationary.

Impact of exercise. We invite a participant to wear MagWear for an hour of detection after running. The heart rate (HR) result is illustrated in Figure 25(c). We observe the HR's MAE is 5.2 bpm when detected at the 10s. The HR's MAE declines with time since that the participant's heartbeat gradually stabilizes after exercise. Finally, the RR's MAE drops to 1.6 bpm after 30min.

Impact of volunteer with high and low blood pressure. Following the IRB regulation, we recruit fifteen volunteers (five with normal BP, five with high BP, and five with low BP) to examine MagWear's performance on them. The result is shown in Figure 25(d). Three groups achieve SBP's MAE of 4.5 mmHg, 3.9 mmHg, 3.2 mmHg and DBP's MAE of 4.1 mmHg, 3.6 mmHg, 3.1 mmHg. We find that the MAE of MagWear is relatively stable for these subjects.

8 RELATED WORK

Physiological sensing with wearables. Existing mainstream wearable devices predominantly employ photoplethysmography (PPG) [32], electrocardiogram (ECG) [33], and inertial measurement unit (IMU) [34] sensors for vital sign monitoring. For instance, devices like Apple Watch, Garmin Watch, and Fitbit leverage PPG sensors to facilitate heartbeat and respiratory detection. Although the PPG has been well explored and validated for everyday usage, it is not without flaws. Notably, PPG sensors have shown sensitivity towards various skin tones, producing biased readings, especially for darker skins [4]. Departing from optical methods, ECG sensors are popular in clinical settings for their robust performance across a diverse range of patients (*e.g.*, skin tones). However, their broader adoption in everyday wearables is limited because they necessitate direct skin contact through electrodes, often attached to the chest. This requirement can be inconvenient for continuous, long-term monitoring. Researchers also explore IMU sensors for physiological sensing. For example, BioWatch [35] employed an IMU sensor within its design to infer physiological signals from pulse-induced vibrations. Extending this concept, [36] examined a chest-mounted IMU to gauge both HR and RR in stationary scenarios. Furthermore, [37] combined PPG and IMU sensors in a smart ring that tracks user activities and estimates HR. However, the IMU's performance can be compromised by skin contact and it may suffer from cumulative drift during long-term monitoring.

Different from the aforementioned works, MagWear delves into an alternative sensing method: biomagnetism. This approach seeks to provide inclusive and long-term physiological monitoring. Preliminary findings with MagWear have demonstrated reliable HR and RR readings across 30 subjects, accounting for variations in skin tones, body hair density, tattoos, clothing fabrics, placement, and moisture conditions.

GMR for vital sign monitoring. The realm of vital sign monitoring has witnessed a burgeoning interest in the potential of biomagnetism [14], [8], [15], [10], [7], [38], [39]. Pioneering studies [8], [10] have validated the capability of GMR sensors in detecting heartbeats when positioned on the wrist in a controlled lab environment. Furthermore, [10] has affirmed the reliability of GMR sensors for RR monitoring by benchmarking their outputs against ECG and PPG data. Concurrently, research in [15] unveiled a groundbreaking non-contact technique for Pulse Wave Velocity (PWV) estimation using GMR sensors, marking a promising avenue for future cardiovascular diagnostics. However, the theoretical capacities and practical boundaries of biomag-

Authorized licensed use limited to: Zhejiang University. Downloaded on October 30,2024 at 06:35:33 UTC from IEEE Xplore. Restrictions apply.
© 2024 IEEE. Personal use is permitted, but republication/redistribution requires IEEE permission. See https://www.ieee.org/publications/rights/index.html for more information.

This article has been accepted for publication in IEEE Transactions on Mobile Computing. This is the author's version which has not been fully edited and
content may change prior to final publication. Citation information: DOI 10.1109/TMC.2024.3452499

netism in human vital sign monitoring remain largely unexplored. Comprehensive understanding and modeling of IBF signals are conspicuously lacking. The challenge of reliably capturing IBF signals amidst human variations remains a significant hurdle.

In contrast to these earlier explorations, MagWear delves deep into the theoretical foundations of IBF signal generation, introduces an adaptive IBF tuning algorithm tailored for diverse human variations, and crafts a wristband designed for daily use. This propels the inclusive vital sign monitoring solution significantly closer to real-world adoption.

9 DISCUSSION

Integrating to existing wearable devices. Our method of estimating blood pressure based on PPT usually requires two channels and these two channels need to be far apart, which is currently a common limitation of this method. Indeed, we admit that it is difficult to directly integrate MagWear BP estimation into existing watches, even though existing watches also hardly support BP estimation. However, we can prototype MagWear as a plug-and-play module that can be used as an accessory or supplement to watches or other wearable devices when BP estimation is needed, thus providing a BP monitoring service. In addition, compared to traditional bandage BP monitors, MagWear is more comfortable to wear. It does not require inflating the arm to create a squeezing sensation, nor does it necessitate frequent user intervention, resulting in a superior user experience.

Applicability to different populations. MagWear provides a general method for vital sign monitoring based on the biomagnetism variation, which is applicable to different populations. Our evaluation also proves that the MAE of MagWear is relatively stable for different subjects. However, from a safety perspective, we suggest that individuals with lower or higher vital signs can use professional medical equipment to enhance vital sign monitoring.

Prone to the human motion. The human motion can affect MagWear's vital sign detection results since the human motion can result in the relative position variation between the GMR sensor and the blood vessel, causing fluctuations in the biomagnetic field detected by the GMR sensor. MagWear is more suitable for continuous vital signs monitoring under the stationary state.

Impact of electromagnetic interference. The electromagnetic interference may affect the MagWear's performance. It is worth noting that the magnetic field strength declines exponentially with the distance. Hence, the influence of electromagnetic interference on MagWear remains constrained, and we can implement a shielding layer to further safeguard the system's external magnets.

The completeness of the dataset. We recruit a total of 30 volunteers including different genders, ages, BMI distributions, and skin tones to collect data following the IRB regulation. Our IRB doesn't mandate specific quotas for recruiting participants and our recruitment process is open to all volunteers. Although the number of volunteers with genders, ages, BMI distributions, and skin tones is not evenly distributed, we hold confidence that our findings will generalize to a more diverse and expansive population. In the future, one may recruit more volunteers, leveraging a larger dataset to make the participant distribution with different skin colors more uniform, to make this technique applied better in practice.

10 CONCLUSION

We present MagWear, the first vital sign monitoring system that practically exploits biomagnetism to achieve heart rate, respiration rate, and blood pressure monitoring. We implement MagWear on COTS low-cost analog components and conduct extensive experiments to evaluate its performance. MagWear explores biomagnetism to achieve heart rate and respiration rate monitoring. Besides, other vital signs are also promising to be detected through the variation of the IBF signal. In essence, the IBF signal is affected by the concentration of charged particles, such as iron and oxygen in the blood vessels. For example, insufficient hemoglobin or ions may lead to the symptoms of anemia and the blood oxygen index can be influenced by the change of oxygen concentration. Hence, we can further explore IBF signal variation to detect anemia and blood oxygen saturation, which is also our ongoing work. We believe that MagWear paves the way for the practical integration of biomagnetism-based vital monitoring systems.

REFERENCES

[1] "All Galaxy Watches," https://www.samsung.com/levant/watches/all-watches/.
[2] "Apple Watch Series 8," https://www.apple.com/apple-watch-series-8/.
[3] "Garmin Sport Watches," https://www.garmin.com/en-US/c/wearables-smartwatches/.
[4] B. Bent, B. A. Goldstein, W. A. Kibbe, and J. P. Dunn, "Investigating sources of inaccuracy in wearable optical heart rate sensors," *NPJ digital medicine*, vol. 3, no. 1, p. 18, 2020.
[5] S. Francesco, C. Gloria, S. Susanna, P. Angelica, I. Grazia, P. Riccardo, B. Alessandro, P. Salvatore, S. Lorenzo, and D. Leonardo, "Photoplethysmograhic sensors, potential and limitations: Is it time for regulation? a comprehensive review," *Measurement*, vol. 218, no. 1, pp. 113–150, 2023.
[6] C. Jeong, H. Yoon, H. Kang, and H. Yeom, "Effects of skin surface temperature on photoplethysmograph," *Journal of Healthcare Engineering*, vol. 5, no. 4, pp. 429–438, 2014.
[7] V. K. Chugh, K. Kalyan, and C. S. Anoop, "Feasibility study of a giant magneto-resistance based respiration rate monitor," in *Proceedings of IEEE EMBC*, 2016.
[8] C. T. Phua, G. Lissorgues, B. C. Gooi, and B. Mercier, "Statistical validation of heart rate measurement using modulated magnetic signature of blood with respect to electrocardiogram," *International Journal of Bioscience, Biochemistry and Bioinformatics*, vol. 2, no. 2, pp. 110–116, 2012.
[9] X. Guo, L. Tan, T. Chen, C. Gu, Y. Shu, S. He, Y. He, J. Chen, and L. Shangguan, "Exploring biomagnetism for inclusive vital sign monitoring: Modeling and implementation," in *Proceedings of the 30th Annual International Conference on Mobile Computing and Networking*, 2024, pp. 1–15.
[10] K. Kalyan, V. K. Chugh, and C. S. Anoop, "Non-invasive heart rate monitoring system using giant magneto resistance sensor," in *Proceedings of IEEE EMBC*, 2016.
[11] D. Cohen, E. A. Edelsack, and J. E. Zimmerman, "Magnetocardiograms taken inside a shielded room with a superconducting point-contact magnetometer," *Applied Physics Letters*, vol. 16, no. 7, pp. 278–280, 1970.
[12] "Introduction of biomagnetism," https://www.sciencedirect.com/topics/biochemistry-genetics-and-molecular-biology/biomagnetism.
[13] "Wheatstone bridge," https://www.geeksforgeeks.org/wheatstone-bridge/.
[14] J. R. Bai and V. J. Kumar, "Optimal design to ensure maximum coupling between magnetic flux and arterial blood in a magneto plethysmo gram sensor head," *IEEE Sensors Journal*, vol. 21, no. 2, pp. 1417–1423, 2021.
[15] A. Chandrasekhar, J. Joseph, and M. Sivaprakasam, "A novel magnetic plethysmograph for non-invasive evaluation of arterial compliance," in *Proceedings of IEEE EMBC*, 2016.
[16] "GMR sensor AA004," https://www.digikey.cn/zh/products/detail/nve-corp-sensor-products/AA004-02E/1624606.
[17] "FDA-approved device, LEPU PO6 fingertip pulse oximeter," https://www.medicalexpo.com/prod/viatom-lepu/product-100940-1010078.html.
[18] N. ui, N. Pham, J. J. Barnitz, Z. Zou, P. Nguyen, H. Truong, T. Kim, N. Farrow, A. Nguyen, J. Xiao, R. Deterding, T. Dinh, and T. Vu, "ebp: A wearable system for frequent and comfortable blood pressure monitoring from user's ear," in *Proceedings of the 25th Annual International Conference on Mobile Computing and Networking*, 2019, pp. 1–17.

Authorized licensed use limited to: Zhejiang University. Downloaded on October 30,2024 at 06:35:33 UTC from IEEE Xplore. Restrictions apply.
© 2024 IEEE. Personal use is permitted, but republication/redistribution requires IEEE permission. See https://www.ieee.org/publications/rights/index.html for more information.

This article has been accepted for publication in IEEE Transactions on Mobile Computing. This is the author's version which has not been fully edited and content may change prior to final publication. Citation information: DOI 10.1109/TMC.2024.3452499

[19] "American National Standards Institute (ANSI) specified error criterion for cardiac monitors and HR meters," https://studylib.net/doc/18662295/ansi-aami-ec13-2002--cardiac-monitors--heart-rate-meters-...

[20] "Hall effect," https://en.wikipedia.org/wikiHall_effect.

[21] "Electromagnetic induction," https://www.techtarget.com/whatis/definition/electromagnetic-induction.

[22] E. J. Kim, C. G. Park, J. Park, S. Suh, C. U. Choi, J. W. Kim, S. Kim, H. E. Lim, S. Rha, H. S. Seo *et al.*, "Relationship between blood pressure parameters and pulse wave velocity in normotensive and hypertensive subjects: invasive study," *Journal of human hypertension*, vol. 21, no. 2, pp. 141–148, 2007.

[23] Y. Ma, J. Choi, A. Hourlier-Fargette, Y. Xue, H. U. Chung, J. Y. Lee, X. Wang, Z. Xie, D. Kang, H. Wang *et al.*, "Relation between blood pressure and pulse wave velocity for human arteries," *Proceedings of the National Academy of Sciences*, vol. 115, no. 44, pp. 11 144–11 149, 2018.

[24] G. Slapničar, N. Mlakar, and M. Luštrek, "Blood pressure estimation from photoplethysmogram using a spectro-temporal deep neural network," *Sensors*, vol. 19, no. 15, p. 3420, 2019.

[25] "Ultra-low power MCU ESP32," https://www.espressif.com/en/products/socs/esp32.

[26] "Instrumentation amplifier INA126," https://www.ti.com/lit/ds/symlink/ina126.pdf.

[27] "Ultralow offset voltage operational amplifier OP07," https://www.analog.com/media/en/technical-documentation/data-sheets/OP07.pdf.

[28] "High-current operational amplifier OPA549," https://www.ti.com.cn/product/cn/OPA549.

[29] "Magnet safety: continuous exposure limits guidelines," https://blink.ucsd.edu/safety/radiation/magnet/limits.html.

[30] D. Chen, M. Wang, C. He, Q. Luo, Y. Iravantchi, A. Sample, K. G. Shin, and X. Wang, "Magx: Wearable, untethered hands tracking with passive magnets," in *Proceedings of the 27th Annual International Conference on Mobile Computing and Networking*, 2021, pp. 269–282.

[31] "Neodymium magnets and pacemaker safety," https://www.kjmagnetics.com/blog.asp?p=pacemaker-safety.

[32] D. Castaneda, A. Esparza, M. Ghamari, C. Soltanpur, and H. Nazeran, "A review on wearable photoplethysmography sensors and their potential future applications in health care," *International journal of biosensors & bioelectronics*, vol. 4, no. 4, p. 195, 2018.

[33] M. Mansoor Baig, H. Gholamhosseini, and M. J. Connolly, "A comprehensive survey of wearable and wireless ecg monitoring systems for older adults," *Medical & Biological Engineering & Computing*, vol. 51, no. 1, pp. 485–495, 2013.

[34] N. Mora, F. Cocconcelli, G. Matrella, and P. Ciampolini, "Fully automated annotation of seismocardiogram for noninvasive vital sign measurements," *IEEE Transactions on Instrumentation and Measurement*, vol. 69, no. 4, pp. 1241–1250, 2020.

[35] J. Hernandez, D. McDuff, and R. W. Picard, "Biowatch: estimation of heart and breathing rates from wrist motions," in *2015 9th International Conference on Pervasive Computing Technologies for Healthcare (PervasiveHealth)*. IEEE, 2015, pp. 169–176.

[36] C. Romano, E. Schena, D. Formica, and C. Massaroni, "Comparison between chest-worn accelerometer and gyroscope performance for heart rate and respiratory rate monitoring," *Biosensors*, vol. 12, no. 10, p. 834, 2022.

[37] H. Zhou, T. Lu, Y. Liu, S. Zhang, R. Liu, and M. Gowda, "One ring to rule them all: An open source smartring platform for finger motion analytics and healthcare applications," in *Proceedings of the 8th ACM/IEEE Conference on Internet of Things Design and Implementation*, 2023, pp. 27–38.

[38] A. J. Lopez-Martin and A. Carlosena, "performance tradeoffs of three novel GMR contactless angle detectors," *IEEE Sensors Journal*, vol. 9, no. 3, pp. 191–198, 2009.

[39] T. Tamori and K. Akatsu, "Investigation of current measurement method of bonding wire by using gmr sensor," in *Proceedings of IEEE ICPE*, 2019.

Xiuzhen Guo is an Assistant Professor with the College of Control Science and Engineering, Zhejiang University. She received her B.E. degree from Southwest University, and her PhD degree from Tsinghua University. Her research interests include wireless networks, Internet of Things, and mobile computing. She is a member of IEEE and a member of ACM.

Long Tan is a PhD student with the College of Control Science and Engineering, Zhejiang University. He received his master's degree from Taiyuan University of Technology (TYUT), Shanxi, China. He received his bachelor's degree from the Hefei University of Technology, Anhui, China. His current research fields include mobile computing and wireless networks.

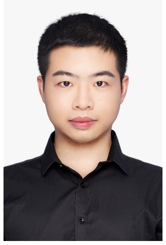

Chaojie Gu (Member, IEEE) received the B.Eng. degree in information security from the Harbin Institute of Technology, Weihai, China, in 2016, and the Ph.D. degree in computer science and engineering from Nanyang Technological University, Singapore, in 2020. He was a Research Fellow with Singtel Cognitive and Artificial Intelligence Lab for Enterprise, in 2021. He is currently an Assistant Professor with the College of Control Science and Engineering, Zhejiang University, Hangzhou, China. His research interests include IoT, industrial IoT, edge computing, and low-power wide area networks.

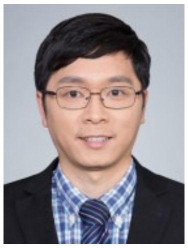

Shibo He (Senior Member, IEEE) received the Ph.D. degree in control science and engineering from Zhejiang University, Hangzhou, China, in 2012. From November 2010 to November 2011, he was a Visiting Scholar with the University of Waterloo, Waterloo, ON, Canada. From March 2014 to May 2014, he was an Associate Research Scientist and from May 2012 to February 2014, a Postdoctoral Scholar with Arizona State University, Tempe, AZ, USA. He is currently a Professor with Zhejiang University. His research interests include Internet of Things, crowdsensing, and Big Data analysis.

Prof. He is on the editorial board of the IEEE TRANSACTIONS ON VEHICULAR TECHNOLOGY, Peer-to-Peer Networking and Applications, and KSII Transactions on Internet and Information Systems. He is also the Guest Editor of Computer Communications and International Journal of Distributed Sensor Networks. He was a Symposium Co-Chair of the IEEE GlobeCom 2020 and IEEE ICC 2017, a TPC Co-Chair of the i-Span 2018, a Finance and Registration Chair of the ACM MobiHoc 2015, a TPC Co-Chair of the IEEE ScalCom 2014, a TPC Vice Co-Chair of the ANT 2013'IC2014, a Track Co-Chair of the Pervasive Algorithms, Protocols, and Networks of EUSPN 2013, a Web Co-Chair of the IEEE MASS 2013, and a Publicity Co-Chair of the IEEE WiSARN 2010 and FCN 2014.

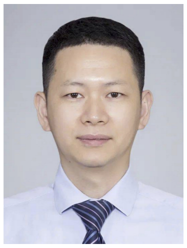

Jiming Chen (Fellow, IEEE) received the PhD degree in control science and engineering from Zhejiang University, Hangzhou, China, in 2005. He is currently a professor with the College of Control Science and Engineering, Zhejiang University. His research interests include IoT, networked control, wireless networks. He serves on the editorial boards of multiple IEEE Transactions, and the general co-chairs for IEEE RTCSA'19, IEEE Datacom'19, and IEEE PST'20. He was a recipient of the 7th IEEE ComSoc Asia/Pacific Outstanding Paper Award, the JSPS Invitation Fellowship, and the IEEE ComSoc AP Outstanding Young Researcher Award. He is an IEEE VTS distinguished lecturer. He is a fellow of the CAA.

Authorized licensed use limited to: Zhejiang University. Downloaded on October 30,2024 at 06:35:33 UTC from IEEE Xplore. Restrictions apply.

© 2024 IEEE. Personal use is permitted, but republication/redistribution requires IEEE permission. See https://www.ieee.org/publications/rights/index.html for more information.